

Thin polymer etalon arrays for high-resolution photoacoustic imaging

Yang Hou

University of Michigan
Department of Electrical Engineering and
Computer Science
1107 Carl A. Gerstacker Building
2200 Bonisteel Boulevard
Ann Arbor, Michigan 48109

Sheng-Wen Huang

Shai Ashkenazi
University of Michigan
Department of Biomedical Engineering
1107 Carl A. Gerstacker Building
2200 Bonisteel Boulevard
Ann Arbor, Michigan 48109

Russell Witte

University of Arizona
Department of Radiology
AHSC
P.O. Box 245067
Building 211, Room 124
1609 N. Warren Avenue
Tucson, Arizona 85724

Matthew O'Donnell

University of Washington
Department of Bioengineering
371 Loew Hall
Box 352180
Seattle, Washington 98195

1 Introduction

Among all medical needs, the ability to detect cancers at early stages¹⁻³ is one of the ultimate goals of virtually every biomedical imaging modality. However, most imaging techniques, including x-ray computerized tomography (CT),^{4,5} ultrasound,^{6,7} and magnetic resonance imaging (MRI),⁸ cannot image small tumors with high specificity. This limitation significantly reduces the probability of successful therapy, since current systems often cannot identify tumors before they reach lethal range. Therefore, it is strongly desired to develop new, noninvasive imaging technologies providing both high contrast and high resolution, preferably in realtime.

Pure optical imaging can produce the high contrast needed because of the vast differences in optical properties within biological tissues. Optical imaging suffers from strong light scattering in tissues, however, resulting in either poor imaging depth, as in optical coherence tomography (OCT),⁹⁻¹¹ or limited imaging resolution, as in diffusive optical tomography (DOT).¹²⁻¹⁴ On the other hand, ultrasound scattering is much

Abstract. Thin polymer etalons are demonstrated as high-frequency ultrasound sensors for three-dimensional (3-D) high-resolution photoacoustic imaging. The etalon, a Fabry-Perot optical resonator, consists of a thin polymer slab sandwiched between two gold layers. It is probed with a scanning continuous-wave (CW) laser for ultrasound array detection. Detection bandwidth of a 20- μm -diam array element exceeds 50 MHz, and the ultrasound sensitivity is comparable to polyvinylidene fluoride (PVDF) equivalents of similar size. In a typical photoacoustic imaging setup, a pulsed laser beam illuminates the imaging target, where optical energy is absorbed and acoustic waves are generated through the thermoelastic effect. An ultrasound detection array is formed by scanning the probing laser beam on the etalon surface in either a 1-D or a 2-D configuration, which produces 2-D or 3-D images, respectively. Axial and lateral resolutions have been demonstrated to be better than 20 μm . Detailed characterizations of the optical and acoustical properties of the etalon, as well as photoacoustic imaging results, suggest that thin polymer etalon arrays can be used as ultrasound detectors for 3-D high-resolution photoacoustic imaging applications. © 2008 Society of Photo-Optical Instrumentation Engineers. [DOI: 10.1117/1.3042260]

Keywords: etalon; optoacoustic detection; photoacoustic imaging; high-frequency ultrasound; high-resolution imaging.

Paper 08018RR received Jan. 15, 2008; revised manuscript received Sep. 8, 2008; accepted for publication Oct. 22, 2008; published online Dec. 23, 2008.

weaker, which consequently yields good resolution at sufficient depth. Conventional ultrasound imaging^{15,16} is based on detection of the compressional properties of tissue; therefore, its contrast is generally weak. A hybrid approach could possibly overcome shortcomings of each by merging the contrast advantages of optical imaging with the resolution advantages of ultrasound imaging. Photoacoustic imaging represents such a hybrid technology.¹⁷⁻²²

Typically, a pulsed laser illuminates the imaging target, where optical energy is absorbed with a distribution corresponding to the optical absorption properties within the desired volume. Acoustic waves are launched by thermoelastic expansion and are measured by ultrasonic transducers placed around the sample in a predetermined geometry. Then the recorded photoacoustic signals are used to reconstruct the image representing the optical absorption distribution. Clearly, the contrast is based on the optical properties of biological tissues, and resolution is scalable with the frequency of the ultrasound waves.

Photoacoustic imaging has seen fast and aggressive growth during the past decade. Successful studies on breast cancer detection,^{20,21} small animal imaging,^{23,24} functional imag-

Address all correspondence to: Yang Hou, Electrical Engineering and Computer Science, University of Michigan 1301 Beal Avenue-Ann Arbor, Michigan 48109 USA; Tel: 7342728069; Fax: 7347631503; E-mail: yang.hou.goblue@gmail.com

ing,^{25,26} and reconstruction algorithms^{27,28} have brought tremendous excitement to this field. Most experimental setups include a pulsed laser and an ultrasound transducer array as the two key elements. The wavelength of the pulsed laser is determined by optimizing both optical penetration depth and optical contrast between cancerous and normal tissues. In most cases, the near-infrared range gives the best trade-off between the two.

Two kinds of ultrasound transducer array are most commonly used in a photoacoustic imaging system. The first uses a piezoelectric transducer array in either 1-D or 2-D arrangements. Generally, these piezoelectric elements operate at frequencies from less than 5 MHz to 20 MHz. The state of the art array system used in photoacoustic imaging is a 1-D 30-MHz array consisting of 48 elements,²⁹ while the best developed for conventional ultrasound imaging include a 64-element 35-MHz 1-D array³⁰ and an 8-element 55-MHz annular array.³¹ Meanwhile, 2-D piezoelectric arrays above 20 MHz are not available for routine use. Recently, capacitive micromachined ultrasound transducer (CMUT) arrays^{32,33} have been tested as possible replacements for piezoelectric arrays and have proved effective in producing 1-D high-frequency arrays up to 45 MHz (Ref. 32).

A second scheme uses a mechanically scanned single element transducer to sweep out the beam direction. This approach is commonly used for high-frequency applications. The low f-numbers of these single-element high-frequency transducers severely restrict imaging depth of field and lead to nonuniform image quality along the axial direction. To improve uniformity, a time-consuming axial mechanical scan is required. Clearly, 2-D ultrasound transducer arrays are highly desired to enable real-time 3-D photoacoustic imaging. However, they are extremely difficult to build with conventional piezoelectric transducers, where the major problems include dicing piezoceramics to micron-scale elements, electrical connections, cross talk between elements, as well as lack of quality high-frequency materials and electronics. Meanwhile, CMUTs require integrated front-end electronics for each independent array element, which is still quite difficult at present. For applications where high frequency and broadband arrays with large element counts are required in simple packages, a new transduction technology is still greatly needed to overcome all these difficulties.

Optical detection of ultrasound has been studied as an alternative to piezoelectric technology for several decades. Passive optical detection is the most straightforward principle, where a laser beam interrogates a transducing surface and ultrasonic displacement causes optical phase shifts. The amplitude of surface motion is typically less than the optical wavelength, thus yielding very small shifts in the optical phase. In reality, the sensitivity of optoacoustic detection must be improved to rival piezoelectricity, and resonant optical ultrasound transducers (ROUTs) have been developed for this purpose.

ROUTs utilize active optical detection and rely on the interaction of the optical field with ultrasound waves in a resonant cavity. External acoustic strain induces modulation of the probe optical field, primarily amplitude instead of phase. With a sharp cavity resonance, the optical response is amplified, which significantly improves sensitivity of optoacoustic detection. ROUTs include etalons,³⁴⁻⁴¹ microrings,^{42,43} fiber

gratings,⁴⁴ and dielectric multilayer interference filters.⁴⁵

One of the simplest and most effective methods utilizes a polymer Fabry-Perot interferometer structure, also known as an etalon.³⁴⁻⁴¹ It is an optical device consisting of a transparent slab sandwiched between two partially reflecting mirrors. Light incident from an external source undergoes multiple beam interference within the etalon and produces a reflected signal intensity that depends on both the optical path length and wavelength. An incident ultrasound wave changes its thickness and resonance condition, thereby modulating the reflected optical intensity when the wavelength is tuned to the maximum slope of the resonance curve. Etalons have been used as ultrasound hydrophones,³⁸ array elements for photoacoustic imaging,⁴¹ and the receiving end of all-optical ultrasound transducers.⁴⁶

Optoacoustic etalons have many advantages over conventional piezoelectric arrays. First, each element is defined by the focal spot of a laser beam; thus, size and spacing of array elements can be reduced to several microns using conventional optics. Second, no electronic connections are needed because optical beams probe elemental signals. Third, improving the bandwidth to 50 MHz or even 100 MHz can be done simply by reducing etalon bulk thickness or choosing the appropriate polymer material. Most importantly, an array can be easily formed by splitting the primary laser beam and focusing the resultant secondary beams onto a configurable array of spots, therefore avoiding the trouble of dicing and assembling the transducing surface.⁴⁷

Up to now, most studies involving etalons have been conducted in the frequency range of 1 to 40 MHz,^{36-41,48,49} where conventional piezoelectric techniques and surging CMUT devices are mature and virtually irreplaceable. Etalons with bandwidths over 50 MHz will significantly expand the frontiers of high-frequency photoacoustic and ultrasound imaging. In minimally invasive applications such as intravascular imaging, the device needs to be integrated onto a guidewire. This approach can significantly limit the size of the array aperture; therefore, higher frequencies above 50 MHz will be required to improve imaging resolution given unfavorable f-numbers. In this paper, we present the development and characterization of high-frequency (>50 MHz) etalon detection arrays especially suited to high-resolution photoacoustic imaging.

2 Structure and Fabrication

An optoacoustic etalon is fabricated by first depositing a 30-nm gold layer on top of a glass substrate using an electron beam evaporator. This gold layer will serve as the first optical reflector. Then, SU-8 photoresist is spin-coated on top at 2100 rpm for 40 s. The cured film is about 5.9 μm thick and forms the etalon's polymer bulk layer. Another 30-nm gold layer is then deposited and will be utilized as the second reflecting mirror. As a final step, an additional 2- μm -thick SU-8 layer is spin-cast over the entire device for protection. A sketch of the side view of the entire etalon structure is shown in Fig. 1(a), and a photo is shown in Fig. 1(b).

The polymer layer thickness can be easily changed by tuning the speed of spin coating. Choosing the proper thickness is a matter of trade-off between sensitivity and bandwidth, as

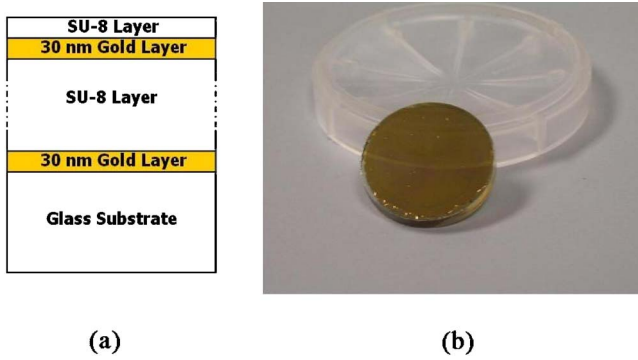


Fig. 1 (a) Sketch of the side view of the etalon structure. (b) Photo of the etalon.

will be discussed later. In this paper, 5.9- μm -thick etalons are investigated unless otherwise specified.

3 Characterization

The optical resonance, acoustic frequency response, noise equivalent pressure, and acoustic angular response of the etalon must be characterized to understand device performance and determine its suitability as a high-frequency ultrasound array detector. The basic experimental setup is shown in Fig. 2. A polarized and collimated continuous-wave (CW) laser beam with power of 4 mW and tunable wavelength from 1440 nm to 1590 nm (Agilent/HP 8168F, Agilent Technologies, Santa Clara, California) travels through a polarized beamsplitter and a quarter wave plate. It is then focused onto a 20- μm spot on the surface of the etalon mounted at the bottom of a water tank. The 20- μm laser focal spot defines a 20- μm ultrasound detection element size. The reflected beam's polarization after traveling through the quarter wave plate is perpendicular to that of the incident beam; therefore, it is reflected off the polarized beamsplitter and is then focused into an amplified InGaAs photodetector connected to the computer for data capture. A piezoelectric transducer is generally placed above the etalon as the source of ultrasound waves.

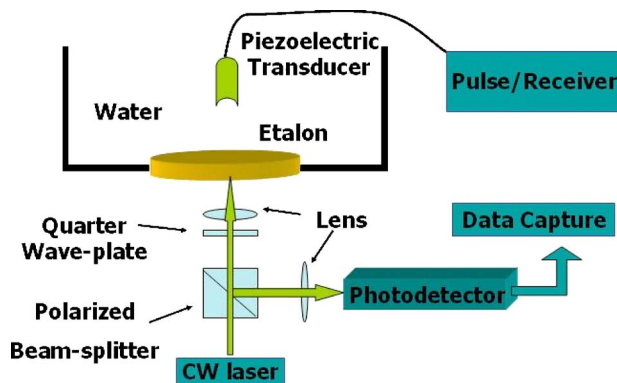


Fig. 2 Block diagram of the experimental setup to characterize the etalon.

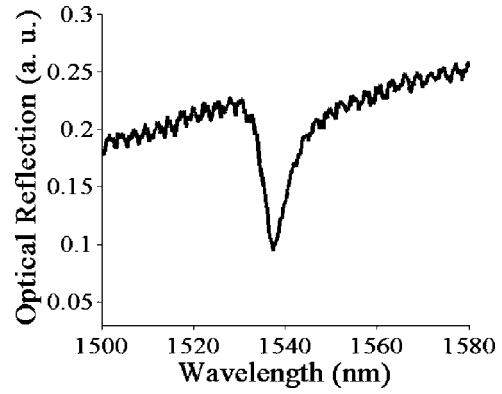


Fig. 3 Optical resonance of the etalon structure.

The reflected optical intensity depends on the optical wavelength,⁵⁰ and displays a sharp drop when the optical path of two-way travel in the etalon bulk equals an integer multiple of the wavelength. This is called the *resonance condition* and creates the mechanism for ultrasound detection. The optical resonance can be measured by recording the reflected optical intensity when the wavelength of the probe CW laser is tuned. As is shown in Fig. 3, the resonance wavelength is 1538 nm with FWHM of 6.3 nm.

The quality factor of the etalon can be estimated to be:⁵⁰

$$Q = \frac{2nd}{\lambda} \cdot \frac{\pi\sqrt{R}}{1-R} \approx 230.$$

Here, $n=1.57$ is the refractive index of SU-8; $d=5.9 \mu\text{m}$ is the thickness of the SU-8 layer; $\lambda=1538 \text{ nm}$ is the resonance wavelength; and $R=0.85$ is the estimated optical reflection coefficient of the two gold layers. The theoretical FWHM of the resonance can be determined using $\Delta\lambda_{1/2}=\lambda/Q \approx 6.6 \text{ nm}$, in good agreement with experimental results. When this device is used for ultrasound detection, the wavelength of the probe laser is tuned to 1536.5 nm, the point of largest slope yielding the largest optical modulation when the resonance condition is changed by the acoustic pressure of the incident ultrasound waves.

The frequency response of the etalon can be calculated using the method developed by Beard and his group.³⁷ Following this approach, the frequency response of the etalon is:

$$|P(f)| \propto \frac{1}{f} \frac{\left| \left[\exp\left(i\frac{2\pi f}{c}l\right) - 1 \right] + R_1 \left[1 - \exp\left(-i\frac{2\pi f}{c}l\right) \right] \right|}{\left| 1 - R_0R_1 \exp\left(-i\frac{2\pi f}{c}2d\right) \right|}. \quad (1)$$

Here, $l=5.9 \mu\text{m}$ is the thickness of the etalon bulk layer, $d=7.9 \mu\text{m}$ is the overall thickness of the etalon, including the protection layer, $c=2500 \text{ m/s}$ is the acoustic velocity in SU-8, and f is the acoustic frequency. R_0 is the acoustic reflection coefficient between SU-8 and water, and R_1 is the coefficient between SU-8 and glass. They can be estimated as the following:

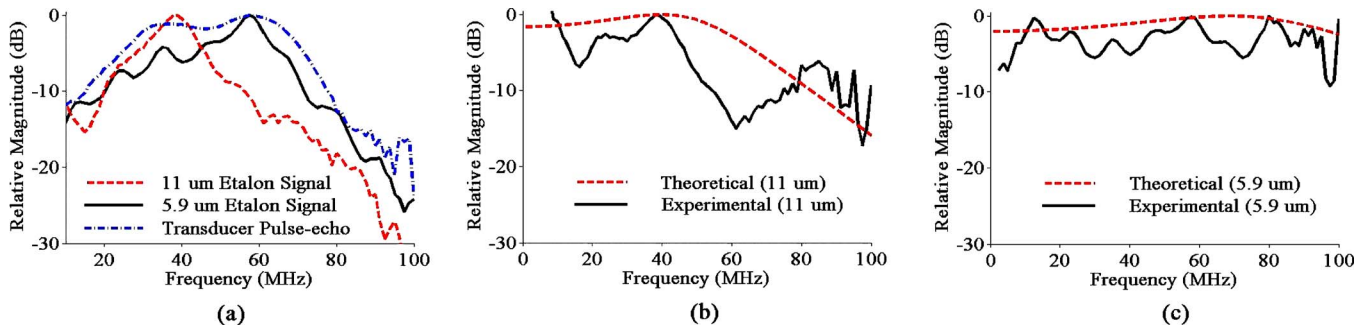


Fig. 4 (a) Spectra of the transducer pulse-echo signal and etalon detection signals from 11- μm and 5.9- μm etalons. (b) Experimental and theoretical acoustic frequency responses of an 11- μm etalon. (c) Experimental and theoretical acoustic frequency responses of a 5.9- μm etalon.

$$R_0 = \frac{Z_{\text{water}} - Z_{\text{SU8}}}{Z_{\text{water}} + Z_{\text{SU8}}} = -0.32, \quad (2)$$

$$R_1 = \frac{Z_{\text{glass}} - Z_{\text{SU8}}}{Z_{\text{glass}} + Z_{\text{SU8}}} = 0.67. \quad (3)$$

Here $Z_{\text{water}} = 1.5 \text{ MRayl}$, $Z_{\text{glass}} = 14.7 \text{ MRayl}$, and $Z_{\text{SU8}} = 2.9 \text{ MRayl}$ are acoustic impedances of water, glass, and SU-8, respectively. The calculated curve is shown in Fig. 4(b) as the dashed line.

Experimentally, the frequency response of the etalon was characterized with a 50-MHz piezoelectric transducer with aperture diameter of 2.5 mm and focal length of 4 mm (LiNbO_3 , Resource Center for Medical Ultrasonic Transducer Technology, University of Southern California). First, a pulse-echo signal reflected from a glass substrate is recorded by the piezoelectric transducer. Then the transducer is placed a focal length away above the etalon, as shown in the setup in Fig. 2, and the signal from the piezoelectric transducer is recorded from the etalon. An 11- μm etalon is also used for comparison purposes.

The frequency response of the etalon is derived by dividing the spectrum of the etalon signal by the square root of the spectrum of the transducer pulse echo. The spectrum of the transducer pulse-echo signal and spectra from both etalons are shown in Fig. 4(a). The derived frequency response of the 11- μm -thick etalon, together with the theoretical curve, is shown in Fig. 4(b). The derived frequency response of the 5.9- μm -thick etalon, and the corresponding theoretical curve, are shown in Fig. 4(c). Clearly, a thinner etalon has a higher frequency response and a broader bandwidth than a thicker one, as illustrated in Fig. 4. These results suggest that the 5.9- μm -thick etalon is suitable for ultrasound detection above 50 MHz.

The noise equivalent pressure of the current system can be measured by replacing the high-frequency transducer in the setup of Fig. 2 with a calibrated 10-MHz transducer (V312, Panametrics NDT, Waltham, Massachusetts). It has a diameter of 6.35 mm and focal length of 19 mm and generates a negative peak pressure of about -2.6 MPa at focus when driven by a commercial pulser/receiver (5077PR, Panametrics NDT, Waltham, Massachusetts). The etalon was put at the focal plane of the transducer. The system outputs a root mean squared noise of 6.4 mV over 25 to 75 MHz with a 32.5-dB

gain amplifier and a peak signal of 101 mV without the amplifier. Therefore, the noise-equivalent pressure (NEP) within the specified 50 MHz bandwidth is estimated to be:

$$\text{NEP} = \frac{2600 \text{ kPa}}{101 \text{ mV}} \times \frac{6.4 \text{ mV}}{42} = 3.9 \text{ kPa}. \quad (4)$$

For an optoacoustic detection element of 20 μm , NEP of 3.9 kPa over a 50-MHz bandwidth is at least as good as, if not significantly better than, polyvinylidene fluoride (PVDF) hydrophones of equivalent size.³⁸ For example, a sensitivity of 6 nV/Pa over a bandwidth of 40 MHz was reported for a 40- μm -diam PVDF needle hydrophone (HP 0.04 mm Interchangeable Probe, HPM04/1, Precision Acoustics Ltd, Dorchester, UK).⁵¹ The output noise level of the preamplifier is 60 μV , which yields an NEP of 10 kPa for this 40- μm PVDF hydrophone. Taking into account the difference in the effective element size and assuming that NEP is inversely linear with area, the NEP of a 20- μm PVDF hydrophone should be 40 kPa, so the etalon is actually much more sensitive than a typical PVDF hydrophone of similar size.

The NEP of the etalon is proportional to the minimum detectable optical power of the photodetector and the Young's modulus of the etalon bulk material and is inversely proportional to the intensity of the etalon probe beam and the quality factor of the etalon (i.e., etalon thickness).³⁷ Increasing the etalon thickness is the easiest way to reduce the NEP. For example, NEP of 2 kPa was measured with 11- μm etalons using the method described earlier. Other straightforward methods to reduce the NEP are to increase the probe beam intensity and increase photodetector sensitivity. Also, the quality factor can be increased by higher optical reflectivity of the two gold layers, which will also contribute to a lower NEP. This has significant implications on photoacoustic imaging applications because extensive averaging can be avoided with better detection sensitivity, thus ensuring real-time imaging.

The same experimental setup as shown in Fig. 2 can be used to measure the angular response of the etalon. A signal generator (8647A, Agilent Technologies, Santa Clara, California) outputs a CW signal at different frequencies (30 to 80 MHz with a 10-MHz step). This signal was gated with a 400-ns pulse (at a pulse repetition rate of 1 kHz) from a wave form generator (33250A, Agilent Technologies) using a frequency mixer (ZFM-4, Mini-Circuits, Brooklyn, New

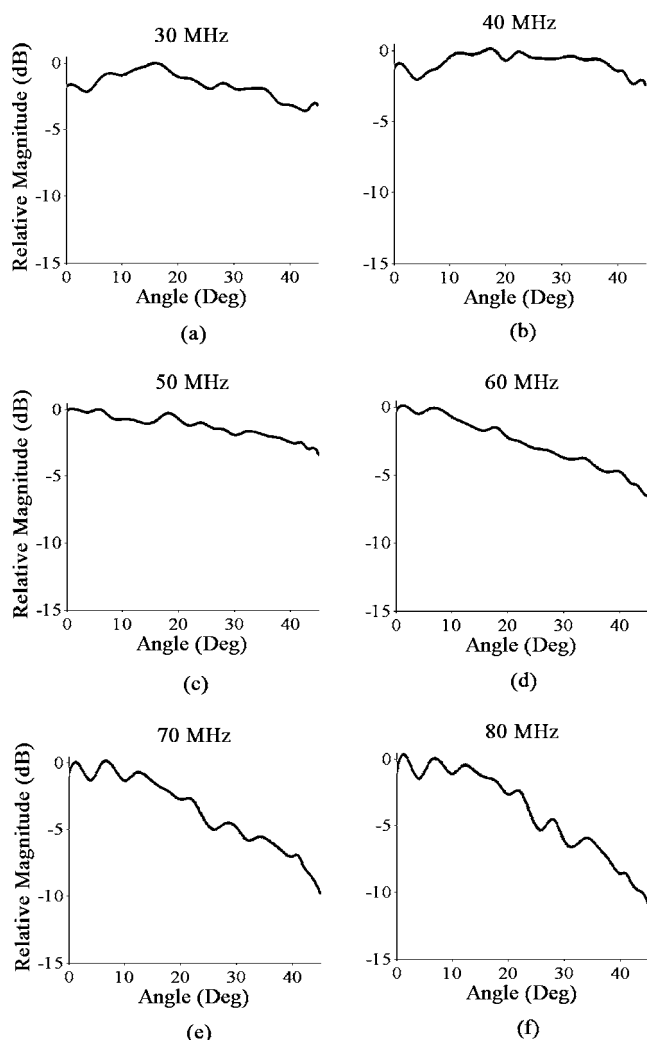


Fig. 5 Angular response from 0 to 45 deg at acoustic frequencies of (a) 30 MHz, (b) 40 MHz, (c) 50 MHz, (d) 60 MHz, (e) 70 MHz, and (f) 80 MHz.

York). The gated CW burst was amplified by a home-made power amplifier (37-dB gain) and then drove a 50-MHz piezoelectric ultrasound transducer (LiNbO_3 , Resource Center for Medical Ultrasonic Transducer Technology, University of

Southern California). The transducer was mounted on a mechanical stage capable of rotation and 3-D translation.

After setting an angle (between the transducer axis and the normal direction of the etalon), the transducer was moved to focus on the active element defined by the optical spot on the etalon surface, and signals corresponding to different (CW) frequencies detected by the etalon were then recorded by an oscilloscope (WaveSurfer 432, LeCroy, Chestnut Ridge, New York). The signal magnitudes at different frequencies and angles from 0 to 45 deg are shown in Fig. 5. Note that at frequencies up to 50 MHz, the relative attenuation at 45 deg compared with 0 deg is only 3 dB, nearly negligible. Only at frequencies above 80 MHz does the attenuation at 45 deg exceed 10 dB. Therefore, the etalon is suitable for high-frequency ultrasound detection even at large angles, making it ideal for photoacoustic imaging applications.

4 Photoacoustic Imaging

Photoacoustic imaging experiments were conducted using the setup shown in Fig. 6(a). The imaging target is placed on the etalon, and a pulsed laser beam illuminates from the side. The laser source is a commercial high-energy solid-state laser at 532 nm (Surelite, Continuum, Inc., Santa Clara, California), which produces a 5-ns laser pulse at repetition rate of 20 Hz. The energy is typically above 100 mJ/pulse and is normally reduced to 10 mJ/pulse using neutral density (ND) filters before hitting the sample. This yields an optical fluence of about 15 mJ/cm^2 , lower than the visible light safety threshold of 20 mJ/cm^2 per pulse (Ref. 52). The probe CW laser beam configuration is the same as that in the characterization experiments (Fig. 2). Therefore, the detection array element size is unchanged at $20 \mu\text{m}$, and the probe power is still 4 mW. The only difference is that all probe beam components are mounted on a 2-D stage, which mechanically scans across the etalon to form a detection array.

Note that the probe beam is scanned, but the etalon remains fixed. This means that any variation in optical resonance characteristic across the imaging aperture will affect ultrasound recordings. Therefore, the CW laser beam is first scanned through the predetermined array geometry to obtain a map of optimal resonance wavelengths. Consequently, during actual ultrasound recordings, the wavelength of the CW laser is automatically tuned to the corresponding optimal resonance

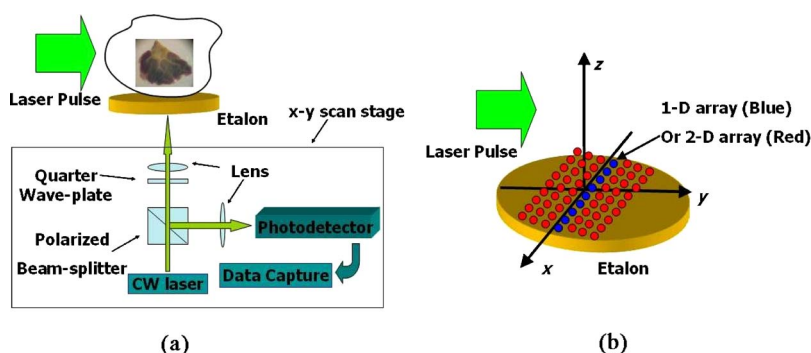


Fig. 6 (a) Experimental setup for photoacoustic imaging using an etalon. (b) Demonstration of 1-D and 2-D detection array configurations. (Color online only.)

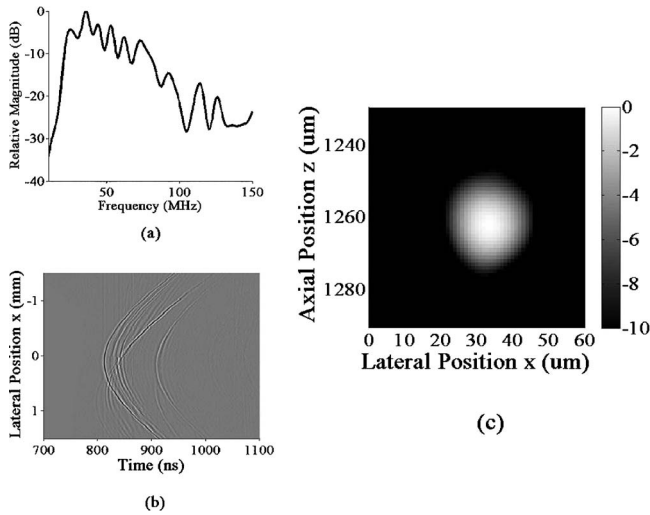


Fig. 7 (a) Spectrum of a typical acoustic signal from a single array element. (b) Wave field plot of the detected acoustic field along a 1-D array. (c) Reconstructed image of the cross section of a 6- μm -diam carbon fiber displayed over a 10-dB dynamic range, where 0 dB represents the maximum reconstructed signal.

wavelength for each array element. Linear scan geometry was chosen because it emulates the ultimate geometry of a fully parallel probe system. Typical scanning configurations are demonstrated in Fig. 6(b), with the red dots illustrating a 2-D array and the blue dots representing a 1-D array, used for 3-D and 2-D imaging, respectively. At each detection position, the signal is averaged 100 times before recording and transfer to the computer for image reconstruction.

A 6- μm -diam carbon fiber embedded in gel phantom is first used as the imaging target. The carbon fiber is positioned parallel to the etalon at a distance of about 1.25 mm from the surface. The detection optical beam is scanned 3 mm in 20- μm steps along the cross section of the carbon fiber. The spectrum of a typical signal is shown in Fig. 7(a). Note that there are a number of interferences in this signal due to the presence of several photoacoustic sources (discussed later). Nevertheless, there is still significant acoustic power at frequencies up to 150 MHz. A bandpass filter from 70 to 150 MHz and demodulation are applied to the recorded signal at each position. Then a conventional delay-sum beam forming algorithm, which involves envelope detection before display to avoid image artifacts resulting from near sidelobes, is used for 2-D image reconstruction. Note that the application of the 70- 150-MHz bandpass filter reduces the SNR of each signal by about 9 dB but still leaves enough for a reasonable dynamic range. A filter in the higher frequency range produces images with better resolution; thus, the specific choice of the bandpass filter is based on the trade-off between resolution and dynamic range.

The wave field plot of the detected acoustic field along this 1-D array is shown in Fig. 7(b), and the reconstructed image is shown in Fig. 7(c). Note that there are other photoacoustic sources in the phantom, as clearly seen from the wave field plot. They represent small optically absorbing objects that were accidentally mixed in the gel. However, these objects are a few hundred microns away from the carbon fiber and there-

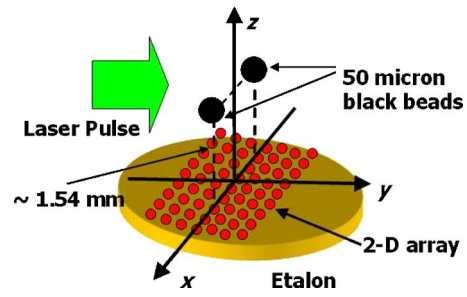


Fig. 8 Experimental configuration with two black beads as imaging targets.

fore do not appear in the reconstructed cross-sectional imaging of the carbon fiber. The lateral FWHM resolution is determined to be 20 μm , and the axial resolution is 19 μm . These results demonstrate that thin polymer etalons are capable of forming detection arrays for photoacoustic imaging at resolutions better than 20 μm , representing one ultrasound wavelength at a frequency of 75 MHz.

The next task is to test a 2-D array for 3-D photoacoustic imaging. A gel phantom containing two 50- μm -diam black beads with centers separated by about 70 μm was used for these studies. The geometrical configuration is shown in Fig. 8. The two beads are placed along the x direction about 1.54 mm above the etalon. The coordinates of their centers are designated as (35, 0, 1540) μm . and (-35, 0, 1540) μm . A photo of these beads on the x - y plane at $z=1540 \mu\text{m}$ is displayed in Fig. 9(a). The detection laser is scanned through a region of 2 mm in x by 2 mm in y , with 20- μm steps in both directions. Bandpass filtering from 35 to 105 MHz was chosen to balance desired resolution and dynamic range. The reconstructed image from the x - y plane at $z=1540 \mu\text{m}$, which contains the centers of the beads, is shown in Fig. 9(b), while those from the y - z plane at $x=35 \mu\text{m}$ (intersection just one bead) and x - z plane at $y=0$

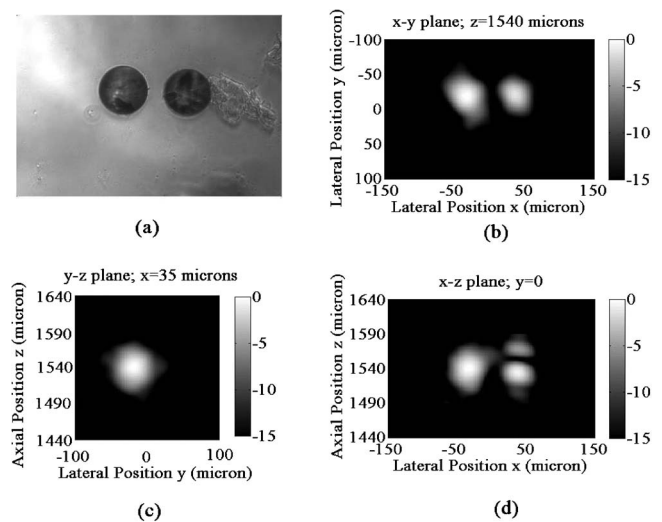


Fig. 9 (a) Photo of two 50- μm -diam black beads. Reconstructed images from the (b) x - y , (c) y - z , and (d) x - z planes displayed over a 15-dB dynamic range, where 0 dB represents the maximum reconstructed signal.

(intersecting both beads) are shown in Fig. 9(c) and 9(d), respectively. These images accurately depict the actual source geometry and confirm the capability of etalons for 3-D photoacoustic imaging.

5 Discussion and Conclusions

Choosing the appropriate thickness is a critical step in fabricating an etalon. As discussed in Sec. 3, thinner etalons produce broader bandwidth, while thicker etalons yield better sensitivity. Determining the optimal thickness is really a matter of trade-off between bandwidth and sensitivity. In our current experimental setup, a 5.9- μm -thick etalon provides bandwidth of well above 50 MHz and NEP of 3.9 kPa. In contrast, an 11- μm -thick etalon has a better NEP of about 2 kPa but is limited to below 40 MHz in bandwidth. Generally, thinner etalons are preferred for two reasons. First, a 2-D array element with higher bandwidth, especially above 50 MHz, is not available with other transducing techniques. Consequently, the number one priority should always be to provide as large a bandwidth as possible. Second, the sensitivity can be easily improved using higher laser power for the probe beam. The results presented here were at optical fluencies far below those that could potentially damage the etalon surface.

At this stage, the focus of the detection laser probes a single array element, and an array is formed by mechanically scanning the detection laser. However, simultaneous detection from all elements in an array system is strongly desired for real-time imaging applications. Our group has taken a big step forward by building a system with an optical end capable of parallel probing,⁴⁷ where an unfocused laser beam probes a large area on the etalon surface, and a photodetector is scanned to acquire signals from all channels. To push this to a realistic imaging device, we have previously proposed a possible scheme^{46,47} where a fiber bundle is used to split the laser into an array of separate laser beams, which are then focused onto a programmable array geometry on the etalon surface. Building a truly parallel array system will certainly be the focus of our future work, with immediate emphasis on fabricating etalons with better thickness uniformity, optimizing the optical setup involving fiber bundles, and evaluating photodetector arrays.

In summary, a 2-D array using thin polymer etalons has been fabricated, characterized, and tested for photoacoustic imaging. A 5.9- μm -thick etalon possesses bandwidth of well over 50 MHz, NEP of 3.9 kPa for a 20- μm -diam element (better than that of PVDF equivalents), and angular attenuation of barely 10 dB at 45 deg for frequencies approaching 80 MHz. Photoacoustic imaging experiments have demonstrated the etalon's utility in 3-D imaging and high-resolution (better than 20 μm) imaging. These results suggest that thin polymer etalons are attractive alternatives to piezoelectric transducers for 3-D high-resolution photoacoustic imaging.

Acknowledgments

This work has been supported in part by NIH under Grant Nos. EB003455, EB003449, and EB004933. The authors gratefully acknowledge the Resource Center for Medical Ul-

trasonic Transducer Technology at the University of Southern California for supplying the high-frequency piezoelectric transducers.

References

1. R. A. Smith, V. Cokkinides, and H. J. Eyre, "American Cancer Society guidelines for the early detection of cancer, 2003," *Ca-Cancer J. Clin.* **53**(1), 27–43 (2003).
2. A. W. H. Lin, N. A. Lewinski, J. L. West, N. J. Halas, and R. A. Drezek, "Optically tunable nanoparticle contrast agents for early cancer detection: model-based analysis of gold nanoshells," *J. Biomed. Opt.* **10**(6), 064035 (2005).
3. U. Pastorino, M. Bellomi, C. Landomi, E. D. Fiori, P. Araldi, M. Picchio, G. Pelosi, P. Boyle, and P. Fazio, "Early lung-cancer detection with spiral CT and positron emission tomography in heavy smokers: 2-year results," *Lancet* **362**, 593–597 (2003).
4. C. I. Henschke, D. I. McCauley, D. F. Yankelevitz, D. P. Naidich, G. McGuinness, O. S. Miettinen, D. M. Libby, M. W. Pasmantier, J. Koizumi, N. K. Altorki, and J. P. Smith, "Early lung cancer action project: overall design and findings from baseline screening," *Lancet* **354**, 99–105 (1999).
5. S. Diederich, D. Wormanns, M. Semik, M. Thomas, H. Lenzen, N. Roos, and W. Heindel, "Screening for early lung cancer with low-dose spiral CT: prevalence in 817 asymptomatic smokers," *Radiology* **222**(3), 773–781 (2002).
6. P. D. DePriest and C. P. DeSimone, "Ultrasound screening for the early detection of ovarian cancer," *J. Clin. Oncol.* **21**(10), 194–199 (2003).
7. A. Blana, B. Walter, S. Rogenhofer, and W. F. Wieland, "High-intensity focused ultrasound for the treatment of localized prostate cancer: 5-year experience," *Urology* **63**(2), 297–300 (2004).
8. K. F. Pirollo, J. Dagata, P. Wang, M. Freedman, A. Vladar, S. Fricke, L. Ileva, Q. Zhou, and E. H. Chang, "A tumor-targeted nanodelivery system to improve early MRI detection of cancer," *Mol. Imaging* **5**(1), 41–52 (2006).
9. T. Q. Xie, M. L. Zeidel, and Y. T. Pan, "Detection of tumorigenesis in urinary bladder with optical coherence tomography: optical characterization of morphological changes," *Opt. Express* **10**(24), 1431–1443 (2002).
10. E. S. Matheny, N. M. Hanna, W. G. Jung, Z. Chen, P. Wilder-Smith, R. Mina-Araghi, and M. Brenner, "Optical coherence tomography of malignancy in hamster cheek pouches," *J. Biomed. Opt.* **9**(5), 978–981 (2004).
11. J. G. Fujimoto, "Optical coherence tomography for ultrahigh resolution *in vivo* imaging," *Nat. Biotechnol.* **21**(11), 1361–1367 (2003).
12. S. R. Arridge and W. R. B. Lionheart, "Nonuniqueness in diffusion-based optical tomography," *Opt. Lett.* **23**(11), 882–884 (1998).
13. J. P. Culver, R. Choe, M. J. Holboke, L. Zubkov, T. Durduran, A. Slemple, V. Ntziachristos, B. Chance, and A. G. Yodanis, "Three-dimensional diffuse optical tomography in the parallel plane transmission geometry: evaluation of a hybrid frequency domain/continuous wave clinical system for breast imaging," *Med. Phys.* **30**(2), 235–247 (2003).
14. B. Pogue, M. Testorf, T. McBride, U. Osterberg, and K. Paulsen, "Instrumentation and design of a frequency-domain diffuse optical tomography imager for breast cancer detection," *Opt. Express* **1**(13), 391–403 (1997).
15. L. Sun, W. D. Richard, J. M. Cannata, C. C. Feng, J. A. Johnson, J. T. Yen, and K. K. Shung, "A high-frame rate high-frequency ultrasonic system for cardiac imaging in mice," *IEEE Trans. Ultrason. Ferroelectr. Freq. Control* **54**(8), 1648–1655 (2007).
16. F. S. Foster, M. Y. Zhang, Y. Q. Zhou, G. Liu, J. Mehi, E. Cherin, K. A. Harasiewicz, B. G. Starkoski, L. Zan, D. A. Knapik, and S. L. Adamson, "A new ultrasound instrument for *in vivo* microimaging of mice," *Ultrasound Med. Biol.* **28**(9), 1165–1172 (2002).
17. M. Xu and L. H. Wang, "Biomedical photoacoustics," *Rev. Sci. Instrum.* **77**(4), 041101 (2006).
18. L. H. Wang, "Ultrasound-mediated biophotonic imaging: a review of acousto-optical tomography and photo-acoustic tomography," *J. Disease Markers* **19**(3), 123–138 (2004).
19. V. Ntziachristos, J. Ripoll, L. H. Wang, and R. Weissleder, "Looking and listening to light: the revolution of photonic imaging," *Nat. Biotechnol.* **23**(3), 313–320 (2005).
20. A. A. Oraevsky, E. V. Savateeva, S. V. Solomatina, A. A. Karabutov,

- V. G. Andreev, Z. Gatalica, T. Khamapirad, and P. M. Henrichs, "Optoacoustic imaging of blood for visualization and diagnostics of breast cancer," *Proc. SPIE* **4618**, 81–94 (2002).
21. A. A. Oraevsky, A. A. Karabutov, S. V. Solomatin, E. V. Savateeva, V. A. Andreev, Z. Gatalica, H. Singh, and R. D. Fleming, "Laser optoacoustic imaging of breast cancer *in vivo*," *Proc. SPIE* **4256**, 6–15 (2001).
 22. D. Lapotko, E. Lukianova, M. Potapnev, O. Aleinikova, and A. A. Oraevsky, "Method of laser activated nano-thermolysis for elimination of tumor cells," *Cancer Lett.* **239**(1), 36–45 (2006).
 23. Y. Xu and L. H. Wang, "Rhesus monkey brain imaging through intact skull with thermoacoustic tomography," *IEEE Trans. Ultrason. Ferroelectr. Freq. Control* **53**(3), 542–548 (2006).
 24. X. Wang, Y. Pang, G. Ku, X. Xie, G. Stoica, and L. H. Wang, "Non-invasive laser-induced photoacoustic tomography for structural and functional imaging of the brain *in vivo*," *Nat. Biotechnol.* **21**(7), 803–806 (2003).
 25. H. F. Zhang, K. Maslov, M. Sivaramakrishnan, G. Stoica, and L. H. Wang, "Imaging of hemoglobin oxygen saturation variations in single vessels *in vivo* using photoacoustic microscopy," *Appl. Phys. Lett.* **90**(5), 053901 (2007).
 26. L. Li, R. Zemp, G. Lungu, G. Stoica, and L. H. Wang, "Photoacoustic imaging of gene LacZ expression in living mice," *J. Biomed. Opt.* **12**(2), 020504 (2007).
 27. M. Xu and L. H. Wang, "Time-domain reconstruction for thermoacoustic tomography in a spherical geometry," *IEEE Trans. Med. Imaging* **21**(7), 814–822 (2002).
 28. Y. Xu, D. Feng, and L. H. Wang, "Exact frequency-domain reconstruction for thermoacoustic tomography—I: planar geometry," *IEEE Trans. Med. Imaging* **21**(7), 823–828 (2002).
 29. R. Zemp, M. Li, R. Bitton, K. K. Shung, G. Stoica, and L. H. Wang, "Photoacoustic imaging of the microvasculature with a high-frequency ultrasound array transducer," *J. Biomed. Opt.* **12**(1), 010501 (2007).
 30. J. M. Cannata, J. A. Williams, Q. Zhou, T. A. Ritter, and K. K. Shung, "Development of a 35-MHz piezo-composite ultrasound array for medical imaging," *IEEE Trans. Ultrason. Ferroelectr. Freq. Control* **53**(1), 224–236 (2006).
 31. E. J. Gottlieb, J. M. Cannata, C. H. Hu, and K. K. Shung, "Development of a high-frequency (>50 MHz) copolymer annular-array, ultrasound transducer," *IEEE Trans. Ultrason. Ferroelectr. Freq. Control* **53**(5), 1037–1045 (2006).
 32. O. Oralkan, S. T. Hansen, B. Bayram, G. G. Yaralioglu, A. S. Ergun, and B. T. Khuri-Yakub, "High-frequency cMUT arrays for high-resolution medical imaging," in *Proc. 2004 IEEE Ultrason. Symp.*, Vol. 1, pp. 399–402 (2004).
 33. O. Oralkan, A. S. Ergun, C. H. Cheng, J. A. Johnson, M. Karaman, T. H. Lee, and B. T. Khuri-Yakub, "Volumetric ultrasound imaging using 2-D CMUT arrays," *IEEE Trans. Ultrason. Ferroelectr. Freq. Control* **50**(11), 1581–1594 (2003).
 34. J. K. Thompson, H. K. Wickramasinghe, and E. A. Ash, "A Fabry-Perot acoustic surface vibration detector—application to acoustic holography," *J. Phys. D* **6**, 677–687 (1973).
 35. J. P. Monchalain, "Optical detection of ultrasound," *IEEE Trans. Ultrason. Ferroelectr. Freq. Control* **33**(5), 485–499 (1986).
 36. P. C. Beard and T. N. Mills, "Extrinsic optical-fiber ultrasound sensor using a thin polymer film as a low-finesse Fabry-Perot interferometer," *Appl. Opt.* **35**(4), 663–675 (1996).
 37. P. C. Beard, F. Perennes, and T. N. Mills, "Transduction mechanisms of the Fabry-Perot polymer film sensing concept for wideband ultrasound detection," *IEEE Trans. Ultrason. Ferroelectr. Freq. Control* **46**(6), 1575–1582 (1999).
 38. P. C. Beard, A. Hurrell, and T. N. Mills, "Characterization of a polymer film optical fiber hydrophone for the measurement of ultrasound fields for use in the range 1 to 20 MHz: a comparison with PVDF needle and membrane hydrophones," *IEEE Trans. Ultrason. Ferroelectr. Freq. Control* **47**(1), 256–264 (2000).
 39. J. D. Hamilton, C. J. Brooks, G. L. Vossler, and M. O'Donnell, "High frequency ultrasound imaging using active optical detection," *IEEE Trans. Ultrason. Ferroelectr. Freq. Control* **45**(3), 719–727 (1998).
 40. J. D. Hamilton, T. Buma, M. Spisar, and M. O'Donnell, "High frequency optoacoustic arrays using etalon detection," *IEEE Trans. Ultrason. Ferroelectr. Freq. Control* **47**(1), 160–169 (2000).
 41. S. Ashkenazi, Y. Hou, T. Buma, and M. O'Donnell, "Optoacoustic imaging using thin polymer etalon," *Appl. Phys. Lett.* **86**, 134102 (2005).
 42. S. Ashkenazi, C. Y. Chao, L. J. Guo, and M. O'Donnell, "Ultrasound detection using polymer microring optical resonator," *Appl. Phys. Lett.* **85**(32), 5418–5420 (2004).
 43. C. Y. Chao, S. Ashkenazi, S. W. Huang, M. O'Donnell, and L. J. Guo, "High-frequency ultrasound sensors using polymer microring resonators," *IEEE Trans. Ultrason. Ferroelectr. Freq. Control* **54**(5), 957–965 (2007).
 44. M. W. Hathaway, N. E. Fisher, D. J. Webb, C. N. Pannell, D. A. Jackson, L. R. Gavrilov, J. W. Hand, L. Zhang, and I. Bennion, "Combined ultrasound and temperature sensor using a fiber Bragg grating," *Opt. Commun.* **171**(4–6), 225–231 (1999).
 45. V. Wilkens, "Characterization of an optical multilayer hydrophone with constant frequency response in the range from 1 to 75 MHz," *J. Acoust. Soc. Am.* **113**(3), 1431–1438 (2003).
 46. Y. Hou, J. S. Kim, S. Ashkenazi, S. W. Huang, L. J. Guo, and M. O'Donnell, "Broadband all-optical ultrasound transducers," *Appl. Phys. Lett.* **97**, 073507 (2007).
 47. S. W. Huang, Y. Hou, S. Ashkenazi, and M. O'Donnell, "High-frequency low-noise ultrasonic detection arrays based on parallelly probing an etalon," in *Proc. 2007 IEEE Ultrason. Symp.*, pp. 719–722 (2007).
 48. S. Ashkenazi, R. S. Witte, K. Kim, S. W. Huang, Y. Hou, and M. O'Donnell, "2D optoacoustic array for high resolution imaging," *Proc. SPIE* **6086**, 60861H (2006).
 49. E. Zhang, J. Laufer, and P. C. Beard, "Backward-mode multiwavelength photoacoustic scanner using a planar Fabry-Perot polymer film ultrasound sensor for high-resolution three-dimensional imaging of biological tissues," *Appl. Opt.* **47**, 561–577 (2008).
 50. M. Born and E. Wolf, *Principles of Optics*, 7th edition, Chapter 7, Cambridge University Press, Cambridge, UK, pp. 360–366 (1999).
 51. "HP 0.04 mm interchangeable probe," <http://www.acoustics.co.uk/products/hpm04-1>.
 52. "Laser Hazards," Chapter 6 in OSHA Technical Manual, http://www.osha-slc.gov/dts/osta/otm/otm_iii/otm_iii_6.html.